Wiener filtering in wall turbulence

Journal of Physics: Conference Series **3230** (2026) 012010 doi:10.1088/1742-6596/3230/1/012010

Wiener filtering in wall turbulence

Marco Castelletti[1], **Federica Gattere**[1] **and Maurizio Quadrio**[1]

[1]Department of Aerospace Science and Technologies, Politecnico di Milano, Milano, Italy

E-mail: marco.castelletti@polimi.it

Abstract.

This work explores the application of control theory to turbulent channel flow. We use linear optimal control theory to design estimators and controllers that use real-time wall measurements to either reconstruct the internal flow field or compute control inputs to reduce drag. A peculiar feature of this study is the use of Wiener filtering, formulated in the frequency domain, which provides a computationally efficient alternative to conventional time-domain design approaches. The proposed framework integrates the best possible (linear) description of both system noise, representing the effect of nonlinear terms neglected by linearization, and linear model of the channel flow. Notwithstanding the highly preliminary nature of this work, we already demonstrate with DNS an interesting amount of drag reduction at $Re_\tau = 200$, and discuss several avenues to further improve control performance.

1 Introduction

Flow control for skin-friction turbulent drag reduction has long been a central goal in fluid mechanics, driven by both fundamental interest and practical applications such as energy-efficient transportation. Over the years, various strategies have been developed, including passive approaches based on geometric modifications and active approaches using actuators. These strategies can be implemented in open- or closed-loop configurations, with the latter driven by real-time flow measurements.

In the context of closed-loop flow control, the linear systems theory offers a rigorous and powerful framework for the design and optimization of control strategies. Although a turbulent flow is highly nonlinear, linear control strategies can be effectively used: suitable linearized models (e.g., the Orr–Sommerfeld–Squire set of equations for parallel flows), while definitely unable to capture the entirety of nonlinear turbulent energy transfer processes, may still be sufficient for effective control, as long as they accurately represent how inputs influence outputs and the associated performance measures [15]. Contrary to the traditional fluid mechanics perspective, a control-oriented model does not need to reliably reproduce the detailed statistics of the uncontrolled flow; instead, it is required to capture the key mechanisms of energy production that flow control for drag reduction seeks to target, as also demonstrated in [5], where linearized equations were employed to explain the turbulence attenuation mechanism induced by an intuition-based closed-loop control strategy. A linear approach to flow control and drag reduction is supported by a substantial body of literature (e.g., [16, 11]), which demonstrates the capability of linear models to control the essential dynamics of the wall turbulence regeneration cycle.

Numerous studies over the past 20-30 years, all based on the Direct Numerical Simulation (DNS) of the Navier–Stokes equations, have been indeed devoted to the estimation and control of wall turbulence within a linear framework. Estimation is the real-time reconstruction of the entire flow field starting from (possibly noisy) wall measurements. Control is designing feedback laws based on wall measurements, and using them to modify the flow dynamics and to achieve the desired objective, e.g. drag reduction (possibly

leading to the relaminarization of the flow). The estimator/controller is based on a linear, time-invariant dynamical system (usually called filter in this context) that provides real-time estimate/control input through filtering the measured signals. The nonlinear terms neglected during the linearization of the Navier–Stokes equations are typically represented via an additive noise.

The most suitable model problem in this context is the turbulent plane channel flow, where the simple geometry makes for a drag entirely made by friction. A linear feedback approach was first presented by [12] for the linear stabilization of two-dimensional laminar plane Poiseuille flow. The linearised model of the flow, i.e. the Orr–Sommerfeld–Squire equations, allows each spatial wavenumber pair to be treated independently: [2] considered a single wavenumber pair, while [9] extended the approach to a large array of wavenumber pairs and applied it to transitional channel flow to stabilize perturbations. The neglected nonlinear terms were substituted by a white noise, i.e., uncorrelated disturbances in time and space, thereby ignoring the actual structure of the nonlinear dynamics. With this approach, in Ref. [8] full-state information was assumed, and an actuation based on wall blowing and suction was shown to successfully relaminarize a turbulent channel flow, although the Reynolds number was highly subcritical at $Re_\tau = 100$, and a gain-scheduling procedure was necessary, to change the controller along the way while the flow evolves from the turbulent towards the laminar state. However, at $Re_\tau = 100$ there is no boundary layer separating the wall from the interior dynamics that support the bulk of the turbulence at higher Re_τ. At higher Reynolds numbers the boundary layer masks the interior flow, making the successful design of a controller based solely on wall-based measurements considerably more challenging. Linear control theory is not the only way to develop controllers; intuition-based controllers, such as the well-known opposition control introduced by [4], and, more recently, complex non-linear controllers based on reinforcement learning techniques, in which the control policy is learned by an agent through trial-and-error interactions with the turbulent channel flow (e.g. [27, 20]), have also been found to be successful in providing drag reduction, as further discussed in 4.2.

As for the estimation, to improve the performance, in a transitional [10] and later a fully turbulent channel flow [3], the true spatial structure of the nonlinear terms was accounted for. The state noise, instead of being assumed a simple white noise, was measured from a DNS of the flow to be controlled in terms of its dependency on the spatial coordinates. However, the noise was still considered white in time, i.e. its time correlation assumed to be a delta function. Results showed that the linear filter could accurately estimate the flow near the wall, but performance degraded quickly further away from it. A more recent example is the work of [1], who designed a linear estimator accounting for the full space–time structure of the disturbances, measured from DNS data. However, their estimator is non-causal — meaning that measurements from the future are required to compute the current estimate — and is therefore unsuitable for real-time applications such as flow control.

All the works cited above, except for [1], developed estimators and controllers using time-domain techniques based on the Kalman theory [14]. While powerful, the time-domain approach is typically formulated for systems driven by white-in-time disturbances and may become computationally demanding for high-dimensional systems. Although colored noise can be accommodated through state augmentation, this often increases the computational burden, motivating alternative formulations in certain settings. Consequently, so far these limitations have prevented linear control from being fully exploited in flow control applications.

Building on the past studies of [23, 24] the present work deals with Wiener filtering. This theory is traditionally developed and applied in the frequency domain, and will be shown here to have the potential to overcome limitations of the standard Kalman theory, thus representing a viable and computationally efficient alternative to the state-space approach, particularly for under-sensed and under-actuated systems such as wall-bounded turbulence, where the number of sensors and actuators is typically much smaller that the number of state variables. The Wiener filtering theory is first briefly introduced in section 2 as the ideal tool to develop optimal linear estimators/controllers within a computationally efficient framework, yielding the best possible linear, time-invariant (LTI) filters for the problem at hand, and dispensing from any additional assumption beyond linearity. We will then focus on a turbulent channel flow at $Re_\tau = 200$, with the numerical setup described in section 3. The Wiener theory is applied to the estimation 4.1 and control 4.2 of the channel flow. A brief concluding discussion on the obtained performance is drawn in section 5.

In this work, the incompressible plane Poiseuille flow between two plane parallel infinite walls is considered. The flow is governed by the incompressible Navier–Stokes equations (iNSE). Streamwise, spanwise and wall-normal directions (velocity components) are indicated with x (u), z (w) and y (v), respectively. Equations are made dimensionless with the bulk velocity U_b and the half height of the channel h, so that $Re_b = U_b h/\nu$ is the Reynolds number, where ν is the fluid kinematic viscosity.

2 Theoretical framework

2.1 Wiener filtering for the estimation problem

An estimator for the state of the flow is designed starting from a linear model of the system, in which modeling errors and uncertainties (here the nonlinear terms) are represented as additive noise entering the state equations. For the turbulent channel flow, following previous work [9], linear estimators are developed using a linearized model obtained from the discretization of the Orr–Sommerfeld–Squire stability equations.

In the following, we will first derive the linear model of the turbulent channel flow and subsequently demonstrate how an optimal linear estimator can be designed efficiently by formulating the problem in the frequency domain.

2.1.1 A linear model for the plant To derive the linear model of the system, the iNSE are rewritten in terms of evolution equations for perturbations about a reference streamwise velocity profile $\bar{u}(y)$, function only of the wall-normal coordinate, as done e.g. in Ref.[3]. In this work, the reference state is always taken as the mean turbulent velocity profile.

The linearized equations can be written in terms of wall-normal velocity and wall-normal vorticity [17] (namely v and $\eta \equiv \partial u/\partial z - \partial w/\partial x$); homogeneity in x and z allows a Fourier series expansion in these directions, leading to:

$$\begin{cases} \dfrac{\partial}{\partial t}\hat{\Delta}\hat{v} + j\alpha\bar{u}\hat{\Delta}\hat{v} - j\alpha\bar{u}''\hat{v} - \dfrac{1}{Re_b}\hat{\Delta}\hat{\Delta}\hat{v} = \hat{h}_v \\ \dfrac{\partial}{\partial t}\hat{\eta} + j\beta\bar{u}'\hat{v} + j\alpha\bar{u}\hat{\eta} - \dfrac{1}{Re_b}\hat{\Delta}\hat{\eta} = \hat{h}_\eta. \end{cases} \tag{1}$$

In the above equations, j is the imaginary unit, α and β are the streamwise and spanwise wavenumbers, hats denote Fourier coefficients, and $\hat{\Delta} = d^2/dy^2 - \kappa^2$ is the Laplace operator, with $\kappa^2 = \alpha^2 + \beta^2$. The prime denotes a derivative in the wall-normal direction, and $\hat{h}_v$ and $\hat{h}_\eta$ are the nonlinear terms, grouped on the right hand side. The system (1) can be rewritten in matrix form, for each wavenumber pair, as:

$$\frac{d}{dt}\underbrace{\begin{pmatrix}\hat{\Delta} & 0\\ 0 & I\end{pmatrix}}_{\mathcal{M}}\underbrace{\begin{pmatrix}\hat{v}\\ \hat{\eta}\end{pmatrix}}_{\hat{q}} + \underbrace{\begin{pmatrix}\mathcal{L}_{OS} & 0\\ j\beta\bar{u}' & \mathcal{L}_{SQ}\end{pmatrix}}_{\mathcal{L}}\begin{pmatrix}\hat{v}\\ \hat{\eta}\end{pmatrix} = \hat{h} \quad \forall\alpha,\beta \tag{2}$$

where $\mathcal{L}_{OS} = j\alpha\bar{u}\hat{\Delta} - j\alpha\bar{u}'' - \hat{\Delta}\hat{\Delta}/Re_b$ and $\mathcal{L}_{SQ} = j\alpha\bar{u} - \hat{\Delta}/Re_b$ are the linear Orr–Sommerfeld and Squire operators. The system of equations (2) inherits the nonlinearity of the Navier–Stokes equations; in fact, evolution equations for each wavenumber pair are coupled to each other via the nonlinear term $\hat{h}$ on the right hand side.

To obtain a linear model, the procedure proposed by Chevalier et al. [3] involves, for each wavenumber pair, dropping the nonlinear terms and replacing them with a noise $\hat{r}$ that possesses the same first- and second-order statistics of $\hat{h}$. In this way, the equations become linear, but the effect of nonlinearity is partially accounted for as the effect of a noise on the state $\hat{q}$. More specifically, $E\{\hat{r}\} = E\{\hat{h}\} = 0$, and the autocorrelation function of $\hat{r}$ is given by

$$R_{\hat{r}\hat{r}}(y_1, y_2, \tau; \alpha, \beta) = E\{\hat{h}(y_1, t+\tau; \alpha, \beta)\hat{h}^H(y_2, t; \alpha, \beta)\}, \tag{3}$$

where $E\{\cdot\}$ is the expectation operator, and the superscript H denotes the Hermitian transpose. Since the wall-normal directions is non-homogeneous, the autocorrelation function explicitly depends on two wall-normal positions; since the flow is statistically steady, only time separation τ appears as independent variable. However, in Ref. [3] the true structure of $\hat{r}$, as given by eq. (3), was considered for the spatial directions only; the time dependence of $\hat{r}$ was not measured, and was simplified by the assumption of white noise in time. Here, instead, we will 'colour' the noise $\hat{r}$ by accounting also for its true full space-time structure as given by eq. (3), which will be measured from DNS data. However, Martinelli [23] shows, as also stated in Ref. [3], that dealing with the temporal structure in the time domain with a Kalman filtering approach is quite inefficient, whereas, a technique based on the frequency domain naturally accounts for it. This is the approach of the present work.

Once the noise $\hat{r}$ is introduced instead of the nonlinear terms, the final form of the linearized governing equations reads

$$\frac{d}{dt}\mathcal{M}\hat{q} + \mathcal{L}\hat{q} = \hat{r} \quad \forall\alpha,\beta. \tag{4}$$

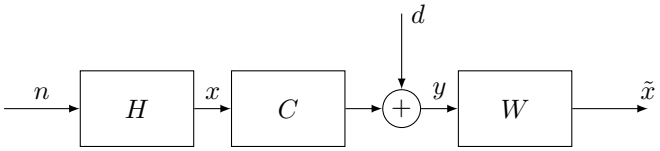

Figure 1: Block diagram of the Wiener filtering estimation problem.

It is a linear model of the system, expressed by a family of partial differential equations in the independent variables y and t, parametrized by the wavenumber pair (α, β). Upon discretization in wall-normal direction, eq. (4) can be recast, for each wavenumber pair, into the standard state-space form

$$\begin{aligned} \dot{x} &= Ax + Br \\ y &= Cx + d \end{aligned} \tag{5}$$

where the hat notation has been omitted for clarity, and the state q has been renamed x following the standard in control theory. The system matrices are given by $A = -\mathcal{M}^{-1}\mathcal{L}$ and $B = \mathcal{M}^{-1}$. Further we introduce the state noise $n = Br$.

The system (5) also introduces the measurement vector y. In a channel flow, measurements should be wall-based quantities, i.e. the two wall-parallel components of the shear stress and the pressure. The measurement matrix C defines how the measured quantities are obtained from the system state x. The term d accounts for measurement noise (such as the electrical noise introduced by any real sensor) and in all the following is assumed to be uncorrelated to the state noise n, as they belong to different physical processes. Further, without loss of generality, the measurement noise will be assumed to be spectrally white, in both space and time. The (large) dimension of the state vector x will be denoted by m, whereas the (small) dimension of the output vector y will be denoted by p_y.

2.1.2 Filter design (in the frequency domain) The estimator can be derived from the LTI system in eq. (5). The filtering problem, illustrated schematically in figure 1, is formulated by following the Wiener theory, i.e. in the frequency domain. As shown in figure 1, the state noise n propagates through the system's frequency response $H(f)$, producing linear perturbations with respect to the reference state, that are represented by the state vector x.

The system frequency response $H(f)$ is the Fourier transform of the system's impulse response function $h(t)$, which is mathematically defined as the matrix exponential of the system matrix A in eq. (5):

$$h(t) = \begin{cases} e^{At}, & t \geq 0, \\ 0, & t < 0. \end{cases} \tag{6}$$

The function $h(t)$ is by definition causal, since it is 0 for $t < 0$. Physically, it describes how the system responds over time to a unit impulse input at $t = 0$, and as such characterizes the linear response of the system to any external excitation. The response function is a building block for any linear system: it links the generic input i to the output o via the time-domain convolution:

$$o(t) = \int_{-\infty}^{+\infty} h(\tau) i(t - \tau) d\tau. \tag{7}$$

In the present problem, the impulse response describes, for each wavenumber pair (α, β), how the flow at a given wall-normal location responds (linearly) to a forcing applied at another specific height and after a certain delay in time.

From the state vector x, a set of measurements is obtained, which are possibly corrupted by additive measurement noise d. By processing these noisy measurements y through a filter yet to be designed, and whose frequency response is $W(f)$, the objective is to reconstruct an estimate $\tilde{x}$ of the true state x.

In designing the filter $W(f)$, the goal is thus to minimize the estimation error $e = \tilde{x} - x$, i.e. the difference between the estimated and the true state. This can be expressed, in frequency domain, through the following cost function:

$$J = \int_{-\infty}^{+\infty} Tr[\phi_{ee}(f)] df,$$

where $\phi_{ee}(f)$ denotes the spectral density of the estimation error, defined as $E\left\{\hat{e}(f)\hat{e}^H(f')\right\} = \phi_{ee}(f)\delta(f-f')$.

From here on, the explicit dependence on the frequency is dropped for clarity. By inspection of the block diagram drawn in figure 1, the state estimation error can be then written as the output of a system driven by n and d as:

$$e = \left(W, \left(WC - I\right)H\right)\begin{pmatrix} d \\ n \end{pmatrix}.$$

Hence, the error spectral density can be recast in the form:

$$\phi_{ee} = W\phi_{dd}W^H + WCH\phi_{nn}H^HC^HW^H + H\phi_{nn}H^H - H\phi_{nn}H^HC^HW^H - WCH\phi_{nn}H^H,$$

where $\phi_{nn}(f)$ and $\phi_{dd}(f)$ denote the spectral densities of n and d. Note that ϕ_{nn} is directly related to correlation appearing in eq. (3), since ϕ_{rr} is the Fourier transform of the correlation function $R_{\hat{r}\hat{r}}$, and $\phi_{nn} = B\phi_{rr}B^H$. The quantity ϕ_{nn} can be measured from DNS data obtained before the design stage, as discussed in section 3, whereas the quantity $\phi_{dd}(f)$ will be considered as a tunable design parameter. The optimal filter W is then one that minimizes the functional:

$$J = \int_{-\infty}^{+\infty} \mathrm{Tr}\left[W\phi_{dd}W^H + WCH\phi_{nn}H^HC^HW^H + H\phi_{nn}H^H - H\phi_{nn}H^HC^HW^H - WCH\phi_{nn}H^H\right]df.$$

This expression highlights what is perhaps the main drawback of the frequency-domain formulation: minimizing this functional yields a non-causal optimal filter, which necessitates future measurements to produce the current estimate. While the filter is guaranteed to be optimal, its non-causality makes it unpractical for real-time control, and usable only in post-processing, unless causality is explicitly enforced. Causality, which is naturally guaranteed in a time-domain approach, translates into the requirement that the frequency response of the filter is a plus function, i.e. that its counterpart in the time domain is zero for $t < 0$. This constraint is enforced by introducing, under the integral operator, an appropriate Lagrange multiplier function $\Lambda_-(f)$ and by modifying the integral (by means of Parseval theorem) as

$$J = \int_{-\infty}^{+\infty} \mathrm{Tr}\big[W_+\phi_{dd}W_+^H + W_+CH\phi_{nn}H^HC^HW_+^H + H\phi_{nn}H^H - H\phi_{nn}H^HC^HW_+^H - W_+CH\phi_{nn}H^H\big] + \mathrm{Tr}[\Lambda_-W_+]\,df.$$

Setting to zero the gradient of J with respect to W_+^H yields:

$$W_+(CH\phi_{nn}H^HC^H + \phi_{dd}) + \Lambda_- = H\phi_{nn}H^HC^H \tag{8}$$

which can be compactly written as:

$$W_+E + \Lambda_- = F, \tag{9}$$

i.e. as a matrix Wiener–Hopf equation.

It is important to notice that the filter's frequency response W_+, the Lagrange multiplier Λ_- and the right hand side F are matrix functions with dimensions $m \times p_y$, whereas the multiplicative coefficient E has dimensions $p_y \times p_y$. Importantly, in eq. (8) the noise spectrum ϕ_{nn} appears explicitly. Therefore, accounting for the true temporal structure of this noise becomes straightforward, and no assumption is required beyond linearity, thus granting that the obtained estimator will be the best possible LTI filter. Furthermore, as demonstrated in section 2.3, the frequency-domain formulation presents interesting computational advantages. As a final remark, solving eq. (8) requires a model of the system in the form of frequency response function $H(f)$. Here $H(f)$ is computed directly from the state-space form of the discretized equation as in eq. (6).

2.2 Wiener filtering for the control problem

The Wiener theory can be applied to derive optimal linear controllers, where the frequency-domain formulation reveals its full potential.

The complete derivation of the controller is omitted here for brevity; while a full paper on it is in preparation, the interested reader is referred to [23], which to our knowledge is so far the only written reference available. In this section, we intend to underscore the main advantages of the approach in comparison to the more popular time-domain formulation; we will also briefly introduce the resulting Wiener–Hopf equation, drawing parallels with eq. 9 obtained in the estimation problem.

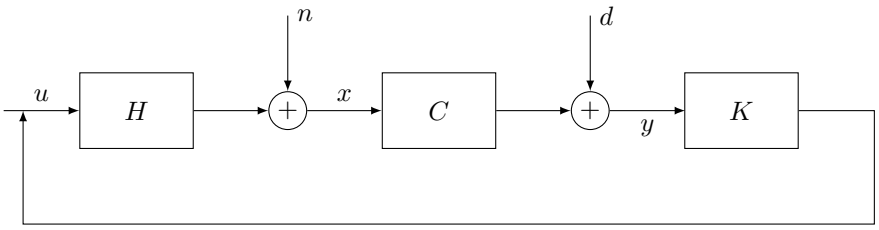

Figure 2: Block diagram of the Wiener filtering feedback control problem.

We consider a multiple-input multiple-output LTI system, with an input-to-state frequency response function $H(f)$ and an output matrix C. The system state and the measurements are respectively affected by state noise n, which represents unmodeled dynamics, and measurement disturbances d. The noises n and d are assumed to be uncorrelated and to possess known statistical properties. It is worth noting that both n and H differ from those defined in the estimation problem shown in figure 1. In the control configuration, the state noise n acts downstream of the system transfer function H, whereas in the estimation problem it enters directly as an input to the dynamics. Here, H represents the flow's response at all wall-normal locations to an impulse of the control input u, whereas in the estimation setting, H gives the response of the flow to the noise corresponding to the dropped nonlinear terms.

The goal is to determine the frequency response function $K(f)$ of the control kernel that, based on real-time measurements y, computes the real-time optimal control input u by minimizing the standard Linear Quadratic Gaussian (LQG) cost functional

$$J = E\{x^H Q x + u^H R u\}, \tag{10}$$

where the first term represents a weighted norm of the system state x (for instance, the turbulent kinetic energy or dissipation in a channel flow), and the second term penalizes control effort. The trade-off between these objectives is governed by the weighting parameter R. The classical block diagram for the feedback control loop is illustrated in figure 2.

The Wiener–Hopf equation to be solved in the control problem is:

$$(H^H Q H + R)\overline{K}_+(C\phi_{nn}C^H + \phi_{dd}) + \Lambda_- = -H^H Q \phi_{nn} C^H. \tag{11}$$

Once this equation is solved for the modified kernel $\overline{K}_+$, the original kernel K can be easily recovered via $K = \overline{K}_+(I + CH\overline{K}_+)^{-1}$.

The filter frequency response $\overline{K}_+$, the Lagrange multiplier Λ_-, and the right-hand side of eq. (11) are matrices of size $p_u \times p_y$, where p_u and p_y are the sizes of the input vector u and the measurements vector y. The matrix multiplying $\overline{K}_+$ on the left has dimensions $p_u \times p_u$, while the one on the right has dimensions $p_y \times p_y$.

Again, as in the estimation problem, the controller derived here represents the best possible LTI controller for the problem under consideration. Notably, unlike eq. (8), none of the matrices in eq. (11) scales with the state dimension m, which is typically much larger than p_y and p_u. This offers a major computational advantage. The frequency domain formulation enables the direct design of the optimal feedback controller in a single step, without invoking the separation theorem. In other words, the controller can be constructed to directly map measurements to control inputs, whereas in the time domain framework one must separately design an optimal estimator and a full-state controller, therefore having to deal at both steps with matrices of order m. This is highly advantageous since, in wall-bounded turbulence the system is typically severely under-sensed and under-actuated ($m \gg p_y, p_u$). The state-space system in eq. (5) is proportional to the number of points discretizing the wall-normal coordinate, and generally has a dimension $m = O(10^{2\text{–}3})$, while at the wall only up to three degrees of freedom are available for actuation and measurement. In the single-input single-output case, eq. (11) reduces to a scalar equation, whereas in the time-domain formulation one would need to solve two Riccati equations involving matrices of size m.

The matrix multiplying $\overline{K}_+$ on the right has the same structure as that in eq. (8). ϕ_{nn} appears again in its functional form, thus allowing the noise n to be easily given its true measured statistics rather than being constrained by the controller dynamics, as in the time-domain approach. The term $C\phi_{nn}$ represents the cross-spectrum between the state noise n and the corresponding measurements. Unlike the spectra

in the estimation problem, which depend on the wall-normal coordinate twice, $C\phi_{nn}$ depends only once on the wall-normal coordinate, making it cheaper to estimate. A final remark concerns the choice of the frequency response function used in the control formulation. Time-domain approaches, such as those of [9, 8], rely directly on the state-space formulation of eq. (5) to derive the controller. Consequently, they implicitly assume a response function that does not account for turbulence fluctuations. In contrast, the present frequency-domain formulation allows the use of any linearized, stable model of the flow system expressed directly in terms of its impulse response function $H(f)$, without the need to convert it into a state-space representation, as required in time-domain methods. This makes it straightforward to employ the averaged linear model of turbulent channel flow proposed by [22]. It consists in the time averaged linear response of the flow to a velocity impulse at the boundary, which bears some similarity with the principal oscillation pattern analysis by [25] and the linear inverse modeling by [6]. It represents the best available linear representation of the turbulent channel flow, as it also accounts, on average, for the effects of turbulent fluctuations and diffusion. Details of its measurements have been more recently provided by [7].

2.3 The numerical solution of the Wiener–Hopf matrix equation

The Wiener–Hopf matrix equation arising in the estimation and control problems can be solved numerically in time domain for the impulse response function of the optimal filter. In fact, inverse Fourier transform of eq. (9) leads to the following system of integral equations:

$$\begin{aligned} \int_0^{+\infty} \mathcal{W}(\tau)\mathcal{E}(t-\tau)\,d\tau = \mathcal{F}(t), \quad t \geq 0 \\ \int_0^{+\infty} \mathcal{W}(\tau)\mathcal{E}(t-\tau)\,d\tau + \mathcal{D}(t) = \mathcal{F}(t), \quad t < 0 \end{aligned} \tag{12}$$

where causality and anticausality of the time domain functions $\mathcal{W}(t)$ and $\mathcal{D}(t)$ has been explicitly used.

The system (12) can be solved in two steps, namely, the first integral equation is solved for the impulse response function $\mathcal{W}(t)$ of the optimal filter; upon substitution in the second equation, the Lagrange multiplier (anticausal) response function $\mathcal{D}(t)$ can be recovered. In the present case, it suffices to solve for the optimal filter impulse response function, which is the quantity of interest. The first integral equation, time-discretized with resolution Δt and truncated on a time window of width $N\Delta t$, can be written, for a generic i-th row of the filter matrix $\mathcal{W}$

$$\Delta t \sum_{k=0}^{N} \mathcal{W}_k^{(i)} \mathcal{E}_{p-k} = \mathcal{F}_p^{(i)}, \quad p = 0, \ldots, N. \tag{13}$$

Taking its conjugate transpose, the previous equation can be rewritten as:

$$\Delta t \begin{pmatrix} \mathcal{E}_0^H & \mathcal{E}_{-1}^H & \cdots & \mathcal{E}_{-N}^H \\ \mathcal{E}_1^H & \mathcal{E}_0^H & \cdots & \mathcal{E}_{-N+1}^H \\ \vdots & \vdots & \ddots & \vdots \\ \mathcal{E}_N^H & \mathcal{E}_{N-1}^H & \cdots & \mathcal{E}_0^H \end{pmatrix} \begin{pmatrix} \mathcal{W}_0^{(i)^H} \\ \mathcal{W}_1^{(i)^H} \\ \vdots \\ \mathcal{W}_N^{(i)^H} \end{pmatrix} = \begin{pmatrix} \mathcal{F}_0^{(i)^H} \\ \mathcal{F}_1^{(i)^H} \\ \vdots \\ \mathcal{F}_N^{(i)^H} \end{pmatrix}.$$

Hence, the filter's impulse response matrix can be constructed row-wise, from the solution of a linear system for each i-th row, $i = 1, \ldots, m$. Note that, from the properties of the multiplicative coefficient E in eq. (9), the matrix to be factored is Hermitian, positive-definite and block-Toeplitz. The factorization can be performed once and for all at the beginning of the procedure, as the matrix does not depend explicitly on the row index. The computational cost of solving the Wiener–Hopf equation scales as $O(N^2)$, and in the single-input single-output case, an even faster algorithm based on the fast Fourier transform (not discussed here) can be used, thus reducing the cost to $O(N \log N)$. This represents a significant improvement compared to the time-domain Riccati-based approach, whose computational cost scales as $O(m^3)$ (note that $N \approx m$).

3 Simulations

The Wiener-based estimation and control are tested on a fully developed turbulent channel flow. We perform direct numerical simulations employing a well-known solver [21]. The code solves the incompressible Navier–Stokes equations in the channel flow, projected in the divergence-free space $v - \eta$. It

Re_τ	L_x	L_y	N_x	N_z	N_y	Δt_{sim}	$\Delta t_{\hat{h}}$	α_m	β_m	N_s	N_{fft}	overlap
200	4π	2π	256	256	200	0.01375	0.4125	8	32	456	256	75%

Table 1: Parameters used in the channel flow simulations and in the construction of the database for the state noise spectra for the stimation problem at $Re_\tau = 200$.

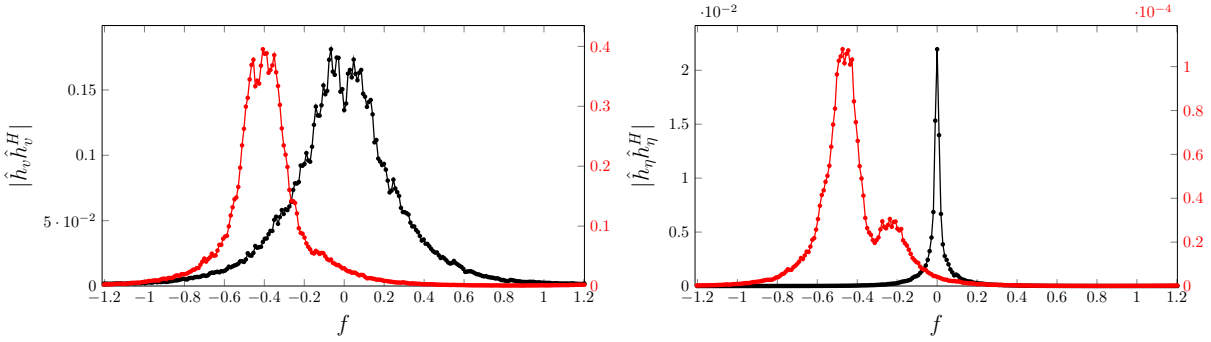

Figure 3: Magnitude of the spectra $E\{\hat{h}_v\hat{h}_v^H\}$ (left) and $E\{\hat{h}_\eta\hat{h}_\eta^H\}$ (right) of the nonlinear terms in the equations for v and η, shown as a function of frequency for two wavenumber pairs: $(\alpha = 0, \beta = 6)$ in black and $(\alpha = 6, \beta = 0)$ in red. Here, $y_1^+ = y_2^+ = 15$.

uses a pseudo-spectral approach, and discretizes the flow variables employing Fourier expansions in the homogeneous streamwise and spanwise directions. Fourth-order accurate, compact and explicit finite difference schemes discretize the differential operators in the wall-normal direction.

The computational domain has size $(L_x,\ L_y,\ L_z) = (4\pi h,\ 2h,\ 2\pi h)$ and is discretized using $N_x = N_z = 256$ Fourier modes in the streamwise and spanwise directions, and $N_y = 200$ wall-normal points. Simulations are run at constant mass flow rate (CFR) at a bulk Reynolds number of $Re_b = 3300$, which correspond to a friction Reynolds number of $Re_\tau \approx 200$, using a constant time step $\Delta t_{sim} = 0.01375$. Unless otherwise indicated, dimensionless quantities are expressed in terms of U_b and h.

For estimation, a preliminary simulation is required to measure the statistics of the state-noise n. Indeed, to solve the Wiener–Hopf equation 8 one needs the spectral density of the state noise ϕ_{rr}, i.e. the Fourier-space counterpart of the correlation function defined in eq. (3) which represents the spectrum of the nonlinear terms appearing on the right-hand side of eq. (1). Once ϕ_{rr} is known, the corresponding state-noise spectrum ϕ_{nn}, appearing in eq. (8), can be computed as $\phi_{nn} = B\phi_{rr}B^H$, as described in section 2.1.

During the preliminary simulation, the time history of the nonlinear term $\hat{h}$ is stored with a time resolution $\Delta t_{\hat{h}} = 0.4125$, which correspond to $\Delta t_{\hat{h}}^+ \approx 5$, where the $+$ superscript indicates scaling in inner (viscous) units. To ensure statistical convergence of the computed spectra, the simulation is run for a total time of $T_{\text{sim}} \approx 10^4$. In order to keep the dimension of the database relatively small, data are stored in the limited wavenumber range $|\alpha| \leq \alpha_m = 8$ and $|\beta| \leq \beta_m = 32$, as also done in Ref. [1].

After the database of the nonlinear terms is available, the spectral density ϕ_{rr} is estimated using the Welch method [29]. The time history is divided into $N_s = 456$ segments of length $N_{fft} = 256$ and an overlap of 75%, whose spectra are averaged together. Each segment is windowed using a Hanning function. As pointed out in Ref. [28], estimation methods based on cross-correlation data require sufficiently long sampling periods. Otherwise, they risk overfitting by 'memorizing' specific flow patterns, yielding good performance within the sampled interval but poor generalization outside it. For this reason, we ensure that the averaging interval used to compute the spectra was sufficiently long. Table 1 summarizes all the simulation parameters employed.

As an example, figure 3 shows the magnitude of the spectra $E\{\hat{h}_v\hat{h}_v^H\}$ (left) and $E\{\hat{h}_\eta\hat{h}_\eta^H\}$ (right), corresponding to the nonlinear terms in the equations for v and η, respectively. This is shown as a function of frequency for two wavenumber pairs, namely $(\alpha = 0, \beta = 6)$ in black and $(\alpha = 6, \beta = 0)$ in red, with $y_1^+ = y_2^+ = 15$ (see eq. 3 for the definition of y_1 and y_2).

For control, the quantities required to solve eq. 11 are the cross-spectrum $C\phi_{nn}$ and the impulse response $H(f)$. Results presented in the following concern a single-input, single-output controller that uses the streamwise component of the wall-shear stress as measurement and the wall-normal velocity at

the wall as control variable. Accordingly, $C\phi_{nn}$ represents the cross-spectrum between the measurement τ_x and the internal velocity components, computed similarly to the estimation problem. For $H(f)$, we use the linear model from [22], representing the average linear response of a turbulent channel flow to wall-normal actuation at the wall, effectively the best possible linear model for this flow. The measurement of this response, described e.g. in [7], requires a long simulation to ensure proper convergence. A thorough description of the procedure to obtain $C\phi_{nn}$ and H is deferred to a future publication.

4 Results

4.1 Estimation

The Wiener filter for estimation is first designed, for each wavenumber pair, by following the procedure outlined in section 2.1, and then tested against a fully nonlinear simulation of a turbulent channel flow. Note that all estimations are carried out using an independent database, distinct from the one used to compute the spectra. Once eq. (8) is solved with the numerical procedure outlined in section 2.3, the impulse response function of the estimation filter $\mathcal{W}(t)$ can be used to retrieve the estimated state $\tilde{x}$ from the measurements m with the convolution integral:

$$\tilde{x}(y,t;\alpha,\beta) = \int_0^t \mathcal{W}(y,\tau;\alpha,\beta)\, m(t-\tau;\alpha,\beta)\, d\tau.$$

The ability of the linear filters to estimate the flow field from wall measurements is assessed in both physical and Fourier space as a correlation between the real and the estimated state. A unitary correlation means perfect estimation of the flow field from wall measurements. Following [3], the correlation in physical space between the true and estimated fields is computed as:

$$\mathrm{corr}(y) = \frac{\int_0^{L_x}\int_0^{L_z} s\tilde{s}\, dx\, dz}{\left(\int_0^{L_x}\int_0^{L_z} s^2\, dx\, dz\right)^{1/2}\left(\int_0^{L_x}\int_0^{L_z} \tilde{s}^2\, dx\, dz\right)^{1/2}}, \tag{14}$$

where $\tilde{s}$ is the quantity estimated with the filter (i.e. the velocity components) and s is its true counterpart (here obtained through DNS). The correlation is also evaluated in wavenumber space, as in [1], as:

$$\mathrm{corr}(y;\alpha,\beta) = \frac{\int \hat{s}(y,t;\alpha,\beta)\, \hat{\tilde{s}}^H(y,t;\alpha,\beta)\, dt}{\left(\int \hat{s}(y,t;\alpha,\beta)^2\, dt\right)^{1/2}\left(\int \hat{\tilde{s}}(y,t;\alpha,\beta)^2\, dt\right)^{1/2}}, \tag{15}$$

where $\hat{s}$ and $\hat{\tilde{s}}$ are the temporal Fourier coefficients of the true and estimated signals at the wavenumber pair (α,β), respectively. This definition extends the physical-space correlation to the spectral domain, making it possible to assess how the estimation error is distributed across streamwise and spanwise wavelengths. The Wiener filters have been designed for an array of wavenumber pairs $|\alpha| \leq \alpha_m$ and $|\beta| \leq \beta_m$, for which ϕ_{nn} was computed. Measurement noise is always assumed to be white, and tests have been performed for different values of the noise intensity.

First, we present the results of the estimation capabilities of the multi-input linear filter, which uses both streamwise and spanwise shear stresses (defined as $\tau_x = \frac{1}{Re_b}\frac{\partial u}{\partial y}\big|_{wall}$ and $\tau_z = \frac{1}{Re_b}\frac{\partial w}{\partial y}\big|_{wall}$) and pressure at the lower wall of the channel as measurements.

Figure 4 shows the correlation coefficient for the three velocity components u (left), w (center), and v (right) through the wall-normal extension of the channel. Solid lines denote filters designed using the full space-time structure of ϕ_{nn}, while dashed lines correspond to filters designed considering white noise in time as done in Ref.[3]. The color scale indicates the level of measurement noise ϕ_{dd}, set at $\phi_{dd} = 10^{-1}, 10^{-3}, 10^{-5}$.

For filters using the full spectral structure, decreasing the measurement noise from 10^{-1} to 10^{-3} leads to higher correlations across all wall-normal distances, particularly near the wall. Further reduction to $\phi_{dd} = 10^{-5}$ yields marginal additional improvement, with correlations approaching unity within the viscous sublayer ($y^+ < 10$). However, regardless of the noise level, the estimator performance deteriorates rapidly away from the wall, and near the channel center the estimated velocities become almost uncorrelated with the true state.

By considering the space-colored time-white filters (dashed lines), one realizes that accounting for the full temporal structure of ϕ_{nn} consistently enhances estimator performance, especially under high measurement noise and for the spanwise and wall-normal velocity components. Nonetheless, for low ϕ_{dd}, the differences are minor. Overall, incorporating the full space-time structure of the noise n improves

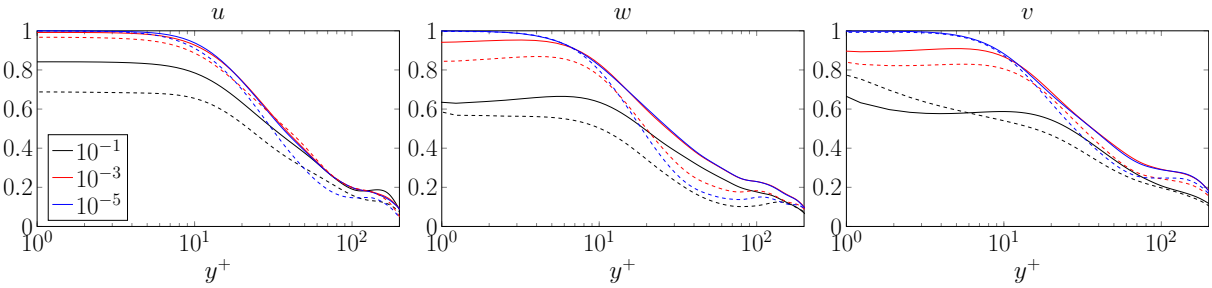

Figure 4: Correlation, computed from eq. (14), between state and wall measurements (two components of wall friction and wall pressure), for different levels of measurements noise ϕ_{dd}, indicated by the line color. streamwise and spanwise stresses and pressure at the lower wall. Left: streamwise velocity; center: spanwise velocity; right: wall-normal velocity. Continuous lines indicate filters which account for the full space-time structure of the nonlinear terms, whereas dashed lines indicate the space-colored time-white filters.

estimation quality but is not a decisive factor: accuracy remains poor far from the wall, consistent with the observations put forward in Ref. [3].

We further compare filters accounting for the full space-time and for only the space spectra by examining instantaneous visualizations of the true and estimated streamwise velocity fields for the case with $\phi_{dd} = 10^{-5}$. This is presented in figure 5 for three wall-normal locations: top, $y^+ \approx 1$; middle, $y^+ \approx 15$; and bottom, $y/h \approx 0.4$. The columns show (left) the true velocity from DNS, (center) the estimate obtained using filters designed with the full temporal structure of ϕ_{nn}, and (right) the estimate from filters where ϕ_{nn} is white in time.

Near the wall, both filters perform well, showing no visible difference from the DNS results. This is expected, as the near-wall velocity structures closely correlate with the wall stresses used as filter inputs. Moving away from the wall, the familiar low-speed streaks become apparent. At $y^+ \approx 15$, both filters successfully capture the overall shape of these structures, with the streak patterns accurately reproduced in both cases, consistent with the strong wall signature of such motions. However, a clear improvement is observed when the full temporal structure of ϕ_{nn} is included: while the time-white filter tends to overpredict velocity maxima, this behavior is corrected when the true temporal correlations are accounted for.

Further from the wall, in the bulk region ($y/h \approx 0.4$), both filters fail to accurately reconstruct the DNS state. Even though incorporating the full temporal structure of the nonlinear forcing noise does enhance estimation, it remains insufficient for an accurate prediction. This result too is not unexpected, as wall measurements are only weakly correlated with the interior flow, making it inherently challenging for a linear estimator to recover the correct state. The estimated fields far from the wall show little resemblance to the true flow, appearing more diffuse and lacking sharp spatial features. Nonetheless, accounting for the true ϕ_{nn} still helps recover significantly more realistic velocity magnitudes.

We conclude the discussion on the multi-input estimation filters by examining the correlation in wavenumber space, eq. (15), to identify which Fourier modes are best estimated. Here, we consider only the filter using the full temporal structure of ϕ_{nn}, with $\phi_{dd} = 10^{-5}$. Figure 6 shows the absolute value of the correlation coefficient for the streamwise velocity at two wall-normal locations: $y^+ \approx 15$ (left) and $y/h \approx 0.3$ (right). Near the wall ($y^+ \approx 15$), most modes are accurately estimated, with performance declining for short streamwise modes combined with relatively large spanwise modes, as well as for modes approaching both α_m and β_m. In contrast, at $y/h \approx 0.3$, only relatively low modes (say $\alpha < 4$ and $|\beta| < 10$) are reasonably captured.

To determine which of the three wall measurements is most informative about the flow, we consider single-input filters. Figure 7 compares the multi-input filter with these single-input filters for a fixed measurement noise level of $\phi_{dd} = 10^{-5}$, which yielded the best performance for the multi-input case. Obviously, the multi-input filter outperforms all single-input filters across all wall-normal locations. Among the single measurements, the streamwise shear stress τ_x is most informative to estimate the streamwise velocity, while the spanwise shear stress τ_z is most informative for estimating both the spanwise and wall-normal velocity components. As reported also in Ref. [1], wall pressure provides the least information among the considered measurements.

Even though we have extended the work of Ref. [3] and designed the best possible LTI filters, by

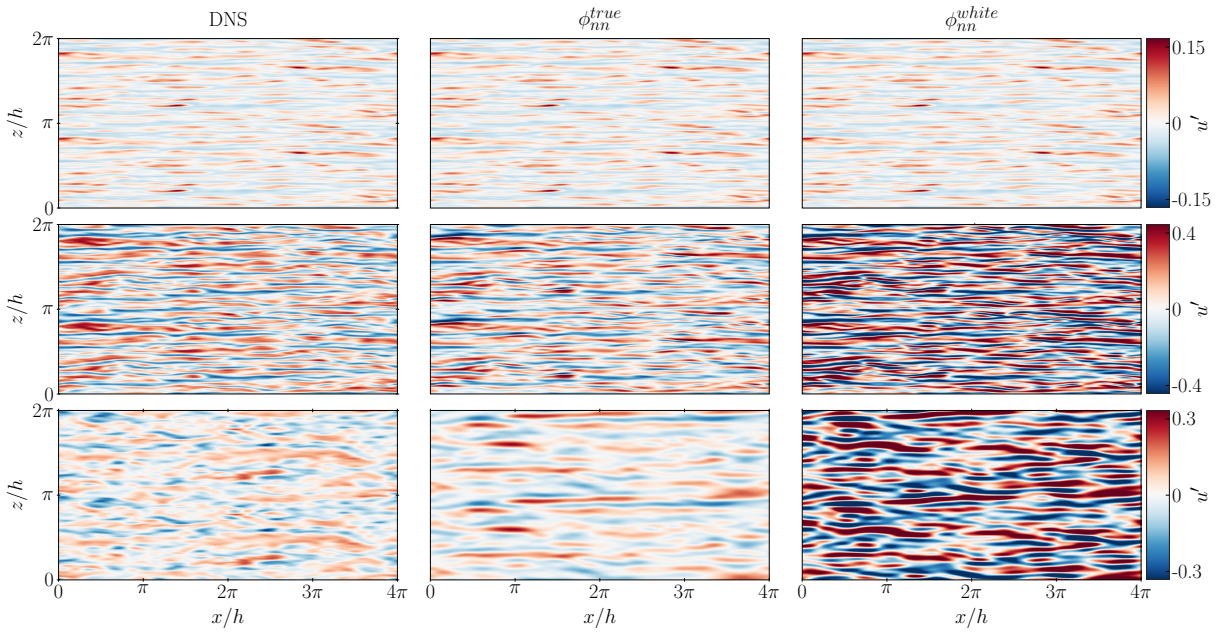

Figure 5: Instantaneous streamwise velocity component from DNS and estimates obtained with the multi-input filter at $\phi_{dd} = 10^{-5}$. Rows correspond to different wall-normal locations: $y^+ \approx 1$ (top), $y^+ \approx 15$ (middle), and $y/h \approx 0.4$ (bottom). Columns show: (left) true DNS field; (center) estimate using the full time structure of ϕ_{nn}; (right) estimate using ϕ_{nn} that is white in time.

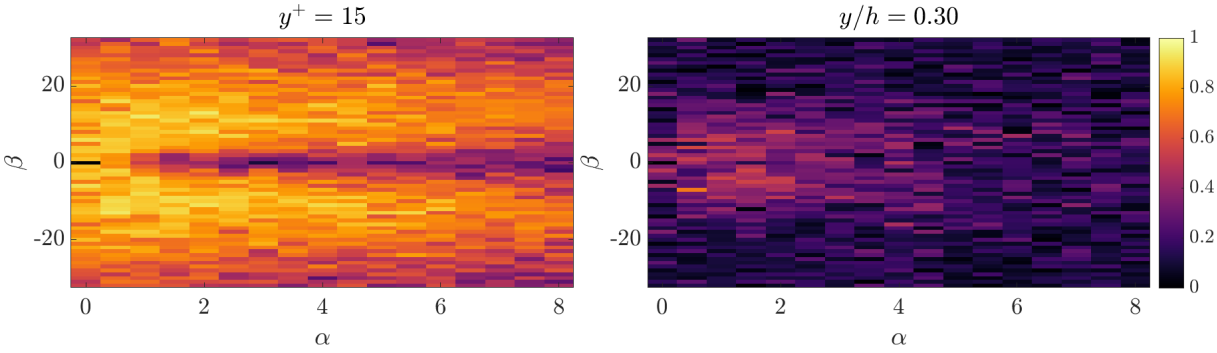

Figure 6: Spectral correlation coefficient of the streamwise velocity (equation 15) for the multi-input filter with $\phi_{dd} = 10^{-5}$ at two wall-normal locations: $y^+ \approx 15$ (left) and $y/h \approx 0.3$ (right).

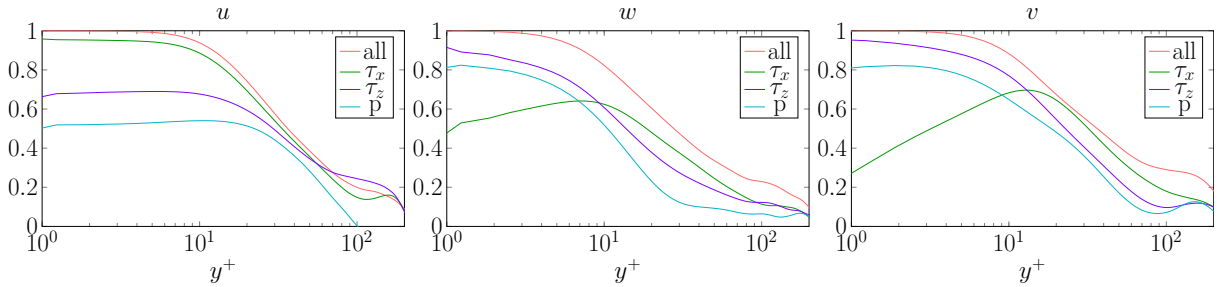

Figure 7: Correlation coefficient for the multi-input filter against single-input ones, for $\phi_{dd} = 10^{-5}$. Left: streamwise velocity; center: spanwise velocity; right: wall-normal velocity.

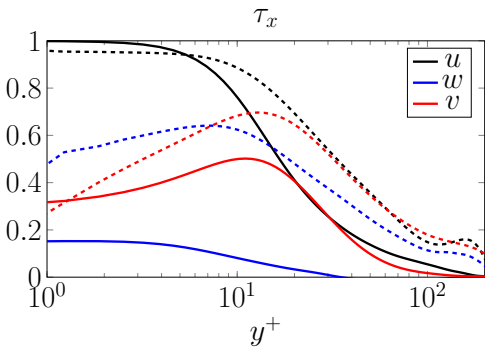

Figure 8: Correlation analysis for a single-input filter using only the streamwise wall-shear stress τ_x. Solid lines: correlation between the measurement τ_x and the internal velocity components. Dashed lines: correlation between the true and estimated velocity components.

accounting for the full space-time structure of the noise, it turns out that such filters are unable to accurately reconstruct the velocity field far from the wall. This limitation is likely related to the fact that the wall contains little to no information about the flow away from it, and the only strategy to possibly circumvent it is to resort to nonlinear filtering.

To better understand this limitation, the correlation between the streamwise wall shear stress τ_x and the internal velocity components is plotted in figure 8: the correlation is very high close to the wall, but deteriorates rapidly going to zero at the center of the channel. Comparing this to the performance of the single-input filter that uses τ_x as a measurement (dashed lines), we observe that the dashed lines nearly always lie above the solid ones, except for u near the wall, where the presence of noise in the design procedure slightly degrades performance. This indicates that the filter incorporates dynamical information beyond what is directly contained in the measurements. The effect is more pronounced for the spanwise and wall-normal velocity components near the wall.

Near the wall, τ_x is strongly correlated with the streamwise velocity u (correlation ≈ 1), whose estimate is only marginally lower. The filter is capable to exploit this accurate estimate of u to improve the prediction of the other components. For instance, the estimated spanwise velocity correlates with the true value at ≈ 0.65, compared to only ≈ 0.2 for the direct correlation with τ_x. However, the estimated correlation profile generally follows that of the correlation between τ_x and the velocity components. As this correlation approaches zero farther from the wall, the filter correspondingly fails to produce accurate estimates.

4.2 Control

We have shown that even the best possible linear estimator can accurately reconstruct the turbulent channel flow only for $y^+ < 20$, and fails to provide reliable estimates farther from the wall. Accounting for the full space-structure of the state noise was indeed beneficial, but not game changing. However, this does not preclude the potential success of linear controllers for wall-bounded turbulence. In fact, wall-based control strategies typically do not require accurate state information far from the wall to achieve drag reduction. This idea is supported by previous studies, such as Ref. [9], which showed that state-feedback control kernels are spatially localized near the actuator region. Other successful, non-feedback drag-reduction techniques, such as the spanwise-oscillating wall [13] and its spatially-inhomogeneous variants [26], attest that significant drag reduction can be achieved by modifying the near-wall flow only. In this section, a preliminary attempt at a linear controller design for drag reduction is presented.

The Wiener filter for the control problem is designed for each wavenumber, following the procedure described in section 2.2. The objective of the control is to reduce viscous drag in turbulent channel flow, and its performance is evaluated in a fully nonlinear DNS.

In this part, we focus on the single-input single-output configuration, where the streamwise wall-shear stress τ_x serves as the measurement, and the wall-normal velocity at the wall (v_{wall}) acts as the control input u. We use as control objective the turbulent dissipation, represented in the cost matrix Q. The choice of turbulent dissipation as cost function is not casual. As shown in [18], unlike the turbulent kinetic energy, the relative contribution of turbulent dissipation to the total dissipation increases with Reynolds number. This suggests that using dissipation as the cost function should provide a more robust

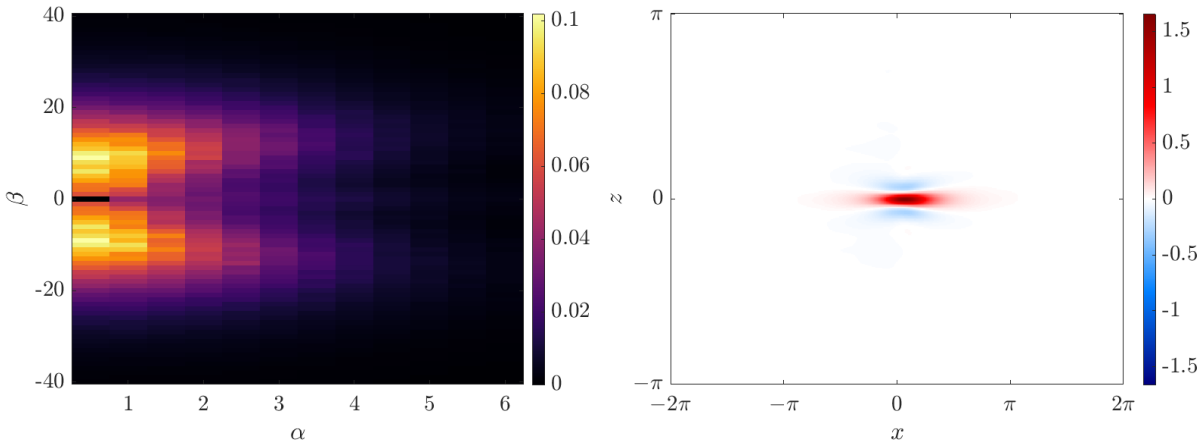

Figure 9: Control kernel K for the single-input single-output case. Measurement is the streamwise wall shear stress τ_x and actuation is via wall-normal velocity imposed at the wall. Left: absolute value of the control kernel in Fourier space at zero time separation, $|\hat{K}(\alpha, \beta, 0)|$, only a fraction of wavenumbers is shown. Right: control kernel in physical space, $K(x, z, 0)$, at zero time separation, illustrating its spatial localization and structure.

metric with respect to an increase in the Reynolds numbers.

Results are presented here for a kernel designed with parameters $R = 0.1$ and $\phi_{dd} = 0.1$. Future work will need to include a parametric investigation to evaluate the effect of different cost functions, measurement, and control inputs, as well as the influence of varying the parameters R and ϕ_{dd}. Crucially, such parameter study will be possible thanks to the computational efficiency of the procedure.

Differently to the estimation problem, where the filter was designed only for a subset of wavenumbers, here the control filter is computed for all the wavenumbers pairs considered in the simulation. Once eq. 11 is solved for the control kernel impulse response $K(t)$, the wall-normal velocity to be imposed at the wall is obtained from the measured τ_x through the convolution integral:

$$v_{wall}(t; \alpha, \beta) = \int_0^t K(\tau; \alpha, \beta)\, \tau_x(t - \tau; \alpha, \beta)\, d\tau.$$

Figure 9 shows the control kernel obtained after solving eq. 11. On the left, the absolute value of the kernel in Fourier space at zero time separation, $|\hat{K}(\alpha, \beta, 0)|$, is plotted as a function of the wavenumber. Note that the plot does not show the range of large α and β where $|\hat{K}(\alpha, \beta, t)|$ is very small. On the right, the kernel is displayed in physical space, $K(x, z, 0)$, again for zero time separation.

Examining the kernel in Fourier space, we observe that it peaks at $\alpha = 0, 1$ and $\beta \approx 8$. In inner units, this corresponds to length scales of $l_x^+ = O(10^3)$ and $l_z^+ = O(10^2)$, which are characteristic of the structures of the well-known near-wall cycle. In physical space, the kernel is well localized, with a large positive peak at the center flanked by two smaller negative peaks on either side. Overall, the kernel exhibits all the desirable properties outlined by Kim and Bewley in Ref. [15]: it is well resolved, it eventually decays at large separations and, if truncated, remains spatially compact with finite support.

The kernel is tested in a fully nonlinear DNS at $Re_\tau = 200$ run for $T_{sim} = 1000$. The control action is updated every $\Delta t = 0.055$ based on real-time measurements of τ_x. Given the preliminary nature of this study, the results are more than encouraging: the turbulent dissipation is reduced by up to 25%, corresponding to a drag reduction $\mathcal{R} = 11\%$. Here, $\mathcal{R}$ is defined as $\mathcal{R} = (C_{f,0} - C_f)/C_{f,0}$, where $C_{f,0}$ is the skin-friction coefficient of the uncontrolled reference flow, and C_f is that of the actuated flow.

It is interesting to examine what is the mechanism by which the present controller achieves drag reduction. In particular, we examine how the control action v_{wall} at a given spatial location correlates with the flow velocity components at various wall-normal heights directly above it.

Figure 10 (a) shows the correlation between the wall-normal control action v_{wall} and the three velocity components: streamwise u (black), wall-normal v (red), and spanwise w (blue), up to $y^+ = 20$. The wall-normal actuation is essentially uncorrelated with the spanwise velocity. In contrast, it exhibits a strong positive correlation with the streamwise velocity, peaking around $y^+ \approx 8$ at approximately 0.9. This

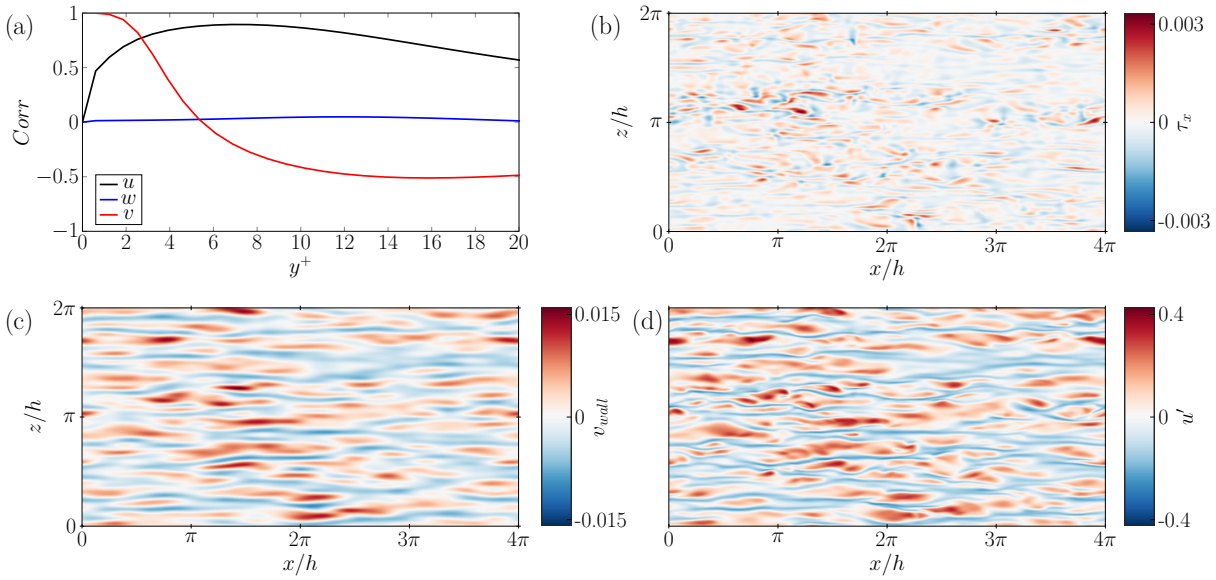

Figure 10: (a) Correlation between the control velocity v_{wall} and the three velocity components: streamwise (u, black), spanwise (w, blue), and wall-normal (v, red) as a function of wall-normal distance y^+. (b) Instantaneous distribution of the wall-shear stress τ_x. (c) Corresponding wall-normal control velocity v_{wall}. (d) Corresponding streamwise velocity fluctuations at $y^+ \approx 8$.

control strategy resembles that obtained by Sonoda et al. [27] with the aid of reinforcement learning, although the wall-normal distance at which the wall blowing relates most to the streamwise fluctuations is different. The imposed v_{wall} also correlates with the vertical velocity component. Near the wall, this correlation is naturally close to 1, since v_{wall} basically correlates with itself. Further from the wall at $y^+ \approx 14$ a negative correlation of about -0.5 emerges, and this suggest that the kernel is deploying an actuation strategy that is reminiscent of the opposition control introduced by Choi et al. in Ref. [4].

Comparing the instantaneous distribution of τ_x at a given time, shown in figure 10(b) with the corresponding wall-normal velocity distribution v_{wall} at the wall in figure 10(c), we observe that the two fields differ significantly (their average correlation coefficient is approximately 0.32). Note that the typical elongated shape of τ_x, which reflects the wall imprint of the streaks, is completely disrupted by the control. However, when comparing v_{wall} with the instantaneous streamwise velocity fluctuations u' at $y^+ \approx 8$, we find a much stronger resemblance. The control field closely follows the spatial structure of u', but presents smoother features, and lacks short-scale features.

Overall, the optimal linear controller presented here combines features of the opposition control [4] and the reinforcement-learning study by Sonoda et al. in Ref. [27]. The lower drag reduction $\mathcal{R}$ observed here is primarily due to the smaller magnitude of v_{wall} compared to previous works. Manual tests increasing the controller intensity showed that larger v_{wall} values distort the expected τ_x distribution, degrading performance and even triggering flow instabilities.

To put these results in perspective, one should start with the observation that feedback controllers which assume that measurements can be taken within the flow achieve larger drag reduction. For example, the so-called opposition control [4], where the wall-normal velocity at the wall is made to oppose vertical velocity fluctuations measured at $y^+ = 10$, achieves drag reductions up to 30%. However, once the restriction that sensors are limited to the wall is introduced, $\mathcal{R}$ shrinks to 6% only. More recently [27] achieved $\mathcal{R} \approx 37\%$ using reinforcement learning with a highly nonlinear control policy based on streamwise velocity fluctuations at $y^+ = 15$ for $Re_\tau = 150$. The resulting controller exhibits an almost binary behavior, applying maximum blowing when the local streamwise velocity fluctuations are positive, and switching sharply to maximum suction when they become negative.

If, instead, we opt for a fairer comparison with feedback control strategies based on wall information and wall control only, the present values of $\mathcal{R}$ are only marginally lower than the best results achieved so far. For instance, [19] achieved $\mathcal{R} \approx 20\%$ using suboptimal linear control theory but at the lower at $Re_\tau = 110$. More recently [20] employing reinforcement learning algorithms up to $Re_\tau = 360$ obtained comparable results with that of [19], at $\mathcal{R} \approx 20\%$. It should be recalled, though, that the present result

is highly preliminary: exploring alternative cost functions, selecting different measurements, and tuning the design parameters, have all the potential for significant improvement of the current performance.

5 Conclusion

In this work, we have designed the ultimate linear estimator and controller for the turbulent channel flow problem. Unlike most previous studies, which relied on time-domain approaches, the present work develops filter and controller design in the frequency domain, using a methodology that is grounded in the Wiener theory.

Formulating the problem in the frequency domain enables a computationally efficient design of the filters that naturally includes all the available flow physics. As discussed in section 2, this approach leads to the best possible optimal linear filter in the sense that, under the assumption of linearity, no further improvement is theoretically possible.

In the first part of this work, we have focused on the estimation problem, i.e. reconstructing the flow field in a turbulent channel through real-time filtering of wall-based measurements. Building upon the previous work by Chevalier et al. [3], who designed a linear estimator considering only the spatial structure of the nonlinear terms, we have extended their approach to incorporate the full space-time structure of these terms. As shown in section 4.1, accounting for the temporal correlations leads to a significant improvement of the estimation performance. Nevertheless, even in this configuration, which represents the best achievable linear estimator, the reconstruction remains accurate only in the near-wall region, and rapidly deteriorates farther from the wall.

In the second part, we have addressed the control problem, where the objective is minimizing friction drag in a turbulent channel flow. In this framework, the designed filter processes in real-time wall measurements to provide an optimal wall distribution of a control variable that minimizes a prescribed cost function. As a preliminary test, we have designed a single-input single-output controller, using the streamwise wall-shear stress as the measurement input and wall-normal blowing and suction as the control output. This configuration achieved a promising friction drag reduction of approximately 11%. Further work is needed on the control side, including the exploration of alternative cost functions, design parameters, and the extension to multiple-input and/or multiple-output configurations.

6 Acknowledgments

This work was supported in part by the European Research Council under the Caust grant ERC-AdG-101018287.

References

[1] F. R. Amaral, A. V. G. Cavalieri, E. Martini, P. Jordan, and A. Towne. Resolvent-based estimation of turbulent channel flow using wall measurements. *J. Fluid Mech.*, 927:A17, November 2021.

[2] T. R. Bewley and S. Liu. Optimal and robust control and estimation of linear paths to transition. *J. Fluid Mech.*, 365:305–349, 1998.

[3] M. Chevalier, J. Höpffner, T. R. Bewley, and D.S. Henningson. State estimation in wall-bounded flow systems. Part 2. Turbulent flows. *J. Fluid Mech.*, 552:167–187, 2006.

[4] H. Choi, P. Moin, and J. Kim. Active turbulence control for drag reduction in wall-bounded flows. *J. Fluid Mech.*, 262:75–110, 1994.

[5] B. F. Farrell and P. J. Ioannou. Turbulence suppression by active control. *Phys. Fluids*, 8(5):1257–1268, May 1996.

[6] B. F. Farrell and Petros J. Ioannou. Statistical state dynamics-based study of the stability of the mean statistical state of wall-bounded turbulence. *Phys. Rev. Fluids*, 9(2):024605, February 2024.

[7] F. Gattere, A. Codrignani, D. Gatti, and M. Quadrio. Potential of the Linear Impulse Response Function of a Turbulent Channel Flow. In *European Fluid Dynamics Conference (EFDC2)*, Dublin (Ireland), 2025.

[8] M. Högberg, T. R. Bewley, and D. S. Henningson. Relaminarization of Reτ=100 turbulence using gain scheduling and linear state-feedback control. *Phys. Fluids*, 15(11):3572–3575, October 2003.

[9] M. Högberg, T.R. Bewley, and D. Henningson. Linear feedback control and estimation of transition in plane channel flow. *J. Fluid Mech.*, 481:149–175, 2003.

[10] J. Höpffner, M. Chevalier, T. R. Bewley, and D.S. Henningson. State estimation in wall-bounded flow systems. Part 1. Perturbed laminar flows. *J. Fluid Mech.*, 534:263–294, 2005.

[11] J. Jimenez. How linear is wall-bounded turbulence? *Phys. Fluids*, 25:110814/20, 2013.

[12] S.S. Joshi, J.L. Speyer, and J. Kim. A systems theory approach to the feedback stabilization of infinitesimal and finite-amplitude disturbances in plane Poiseuille flow. *J. Fluid Mech.*, 332:157–184, February 1997.

[13] W.J. Jung, N. Mangiavacchi, and R. Akhavan. Suppression of turbulence in wall-bounded flows by high-frequency spanwise oscillations. *Phys. Fluids A*, 4 (8):1605–1607, 1992.

[14] R. E. Kalman. A New Approach to Linear Filtering and Prediction Problems. *J. Basic Eng*, 82(1):35–45, March 1960.

[15] J. Kim and T.R. Bewley. A linear systems approach to flow control. *Annu. Rev. Fluid Mech.*, 39:383–417, 2007.

[16] J. Kim and J. Lim. A linear process in wall-bounded turbulent shear flows. *Phys. Fluids*, 12(8):1885–1888, 2000.

[17] J. Kim, P. Moin, and R. Moser. Turbulence statistics in fully developed channel flow at low Reynolds number. *J. Fluid Mech.*, 177:133–166, 1987.

[18] F. Laadhari. Reynolds number effect on the dissipation function in wall-bounded flows. *Phys. Fluids*, 19(038101), 2007.

[19] C. Lee, J. Kim, and H. Choi. Suboptimal control of turbulent channel flow for drag reduction. *J. Fluid Mech.*, 358:245–258, 1998.

[20] T. Lee, J. Kim, and C. Lee. Turbulence control for drag reduction through deep reinforcement learning. *Phys. Rev. Fluids*, 8(2):024604, February 2023.

[21] P. Luchini and M. Quadrio. A low-cost parallel implementation of direct numerical simulation of wall turbulence. *J. Comp. Phys.*, 211(2):551–571, 2006.

[22] P. Luchini, M. Quadrio, and S. Zuccher. Phase-locked linear response of a turbulent channel flow. *Phys. Fluids*, 18(121702):1–4, 2006.

[23] F. Martinelli. *Feedback Control of Turbulent Wall Flows*. PhD thesis, Politecnico di Milano, 2009.

[24] F. Martinelli, M. Quadrio, and P. Luchini. Turbulent drag reduction by feedback: A Wiener-filtering approach. In B. Eckhardt, editor, *Advances in Turbulence XII, Proc. 12th EUROMECH Eur. Turbulence Conf., Marburg (D), Sept. 2009. ISBN 978-3-642-03084-0*, volume 132 of *Springer Proceedings in Physics*, pages 657–660. Springer Berlin Heidelberg, 2009.

[25] C. Penland. Random Forcing and Forecasting Using Principal Oscillation Pattern Analysis. *Monthly Weather Review*, 117(10):2165–2185, October 1989.

[26] M. Quadrio, P. Ricco, and C. Viotti. Streamwise-traveling waves of spanwise wall velocity for turbulent drag reduction. *J. Fluid Mech.*, 627:161–178, 2009.

[27] T. Sonoda, Z. Liu, T. Itoh, and Y. Hasegawa. Reinforcement learning of control strategies for reducing skin friction drag in a fully developed turbulent channel flow. *J. Fluid Mech.*, 960:A30, April 2023.

[28] T. Suzuki and Y. Hasegawa. Estimation of turbulent channel flow at Retau=100 based on the wall measurement using a simple sequential approach. *J. Fluid Mech.*, 830:760–796, November 2017.

[29] P. Welch. The use of fast Fourier transform for the estimation of power spectra: A method based on time averaging over short, modified periodograms. *IEEE Trans. Audio Electroacoust.*, 15(2):70–73, June 1967.